PAPER

Check for updates

Green transformation of biomass-derived Indian gooseberry into fluorescent intrinsic nitrogen-functionalized carbon quantum dots for real-time detection of vitamin B$_2$ in the nanomolar range†

Mandeep Kaur, Mily Bhattacharya [iD]* and Banibrata Maity [iD]*

Riboflavin (RF) detection is essential for controlling nutritional health due to its increasing significance in the food and pharmaceutical industries. Regular daily intake of RF (vitamin B$_2$) is important because it is not synthesized and stored in the human body in appreciable amounts. Therefore, an efficient and biocompatible nanosensor with good selectivity and sensitivity for RF detection is required. Carbon quantum dots (CQDs) derived from biomass have recently attracted interest in environmental science due to their simple, cost-effective methods of synthesis, as well as their sustainability advantages and practical implications. Herein, we demonstrate the utility of a ratiometric fluorescence-based CQD nanosensor for the detection of RF in its isolated, pure form as well as in pharmaceutical tablets. We report the synthesis, characterization, and sensing potential of intrinsic nitrogen-functionalized carbon quantum dots (N-CQDs) from Indian gooseberry (a renewable biomass precursor) using a microwave-assisted pyrolysis method that involves a green methodology and occurs rapidly. High-resolution transmission electron microscopy (HRTEM) indicated that N-CQDs are monodisperse with an average diameter of ∼8.1 nm. Fourier-transform infrared (FTIR) and X-ray photoelectron spectroscopy (XPS) validated intrinsic nitrogen functionalization and the presence of amino, hydroxyl, and carboxyl groups on the surface of N-CQDs. Further, X-ray diffraction (XRD), UV-visible and fluorescence spectroscopy, and time-correlated single photon counting (TCSPC) measurements were also employed for the characterization of N-CQDs. The as-prepared nanoprobe exhibits bright green emission with a remarkable fluorescence quantum yield of 48%. Moreover, N-CQDs are highly water-soluble and are extremely stable across a range of pH, ionic strength, and light. Additionally, N-CQDs selectively and specifically detect RF (vitamin B$_2$) in aqueous media w.r.t various bio-analytes with a limit of detection (LOD) ∼35 nM. Our nanosensor can also detect vitamin B$_2$ present in commercially available pharmaceutical tablets with an LOD of ∼61 nM. Mechanistic studies confirmed that sensing involves fluorescence resonance energy transfer (FRET) between RF and N-CQD interfaces. Overall, the present work provides a new vision for the development of an innovative and sensitive approach of a green fluorescent nanosensor for the detection of RF which may find potential applications in the pharmaceutical and food industries.

Department of Chemistry and Biochemistry, Thapar Institute of Engineering and Technology, Patiala 147004, India. E-mail: mily.bhattacharya@thapar.edu; banibrata.maity@thapar.edu; mkaur3_phd19@thapar.edu

† Electronic supplementary information (ESI) available: Fig. S1 shows the HR-TEM image of N-CQDs and the EDS spectra of N-CQDs. Fig. S2 displays changes in fluorescence emission spectra of N-CQDs at different excitation wavelengths along with normalized fluorescence emission spectral shifts in HEPES buffer at pH 7.4. Fig. S3 depicts the zeta potential of N-CQDs, fl. intensity of N-CQDs in aqueous and HEPES buffer at pH 7.4, impact of ionic strength at different concentrations of NaCl (0–2 M) and irradiation time of N-CQDs and photograph demonstrating utility of N-CQDs as a fluorescent ink. Fig. S4 depicts the variation in fluorescence spectra of N-CQDs in the presence of different concentrations of RF (0–2.2 μM) in HEPES buffer at pH 7.4 and a real sample of vitamin B$_2$. Fig. S5 shows the Stern–Volmer plots of N-CQDs in an aqueous medium, HEPES buffer at pH 7.4, and a real sample

of vitamin B$_2$ respectively. Fig. S6 depicts the Benesi–Hildebrand plot of N-CQDs in an aqueous medium, HEPES buffer medium at pH 7.4, and a real sample of vitamin B$_2$ respectively. Fig. S7 shows the spectral overlap between the emission spectrum of N-CQDs and the excitation spectrum of RF and fluorescence lifetime decays of N-CQDs in the presence of RF in HEPES buffer at pH 7.4 and a real sample of vitamin B$_2$. Fig. S8 shows the linear relationship of the fluorescence response (F_0/F) of N-CQDs with different concentrations of RF (0–2.2 μM) in HEPES buffer at pH 7.4 and a real sample of vitamin B$_2$. Table S1 includes details of various parameters obtained during the deconvolution of the XPS data. Table S2 includes the fluorescence lifetime components of N-CQDs and their respective coefficients along with the mean fluorescence lifetimes in aqueous and pH 7.4 medium. Table S3 represents the application of the developed nanosensor for detection of real samples of RF in tablets. See DOI: https://doi.org/10.1039/d3su00456b

Sustainability spotlight

Vitamin B$_2$ is an essential water-soluble vitamin for human health yet, is neither generated nor stored in significant amounts in the human body. Therefore, regular consumption of vitamin B$_2$-rich food items is required as its deficiency causes various diseases. Since good health and well-being at all ages is one of the goals of UN SDGs, hence, development of a simple-cum-reliable method for determining vitamin B$_2$ concentration in various foods and human blood is necessary. We report selective-and-specific sensing of vitamin B$_2$ by our synthesized nanoprobe (nitrogen-functionalized carbon quantum dots) from Indian gooseberry using a green methodology. We believe our work aligns with the transformation of biomass into non-toxic, high-value products that also address several environmental and renewable energy concerns.

1. Introduction

Riboflavin (RF), commonly known as vitamin B$_2$, is an essential water-soluble vitamin for human health. All the flavoproteins need RF as most of it is converted to its cofactor forms namely, flavin adenine dinucleotide (FAD) and flavin mononucleotide (FMN). Additionally, RF is required for protein, lipid, carbohydrate, and ketone metabolism, as well as during electron transport processes in the respiratory chain. In human beings, RF serves as an antioxidant, combating free radicals and protects against cancer. Since vitamin B$_2$ is neither generated nor stored in significant amounts in the human body, regular consumption of the vitamin through various RF-rich food items such as milk, yogurt, cereals, pork, eggs, almonds, fresh green vegetables, and dairy products, is considered to be essential. Deficiency of RF causes mucocutaneous infections, anemia, fatigue, acute photophobia, delayed growth, angular cheilitis, cardiovascular and digestive issues, seborrheic dermatitis, scrotal cheilosis, vulvar skin abnormalities, and many more. Therefore, it is essential to have a simple and reliable method for determining the concentration of RF in various foods, vitamin B$_2$ supplements, human blood, and metabolic processes.[1-5] The conventional methods for detecting riboflavin in foods, pharmaceuticals, and supplements include high-performance liquid chromatography (HPLC), capillary electrophoresis, ultraviolet-visible spectroscopy (UV-vis), electrochemical approaches, immunoassay colorimetric approach, molecular imprinting *etc.* Most of these methods have a variety of shortcomings, including lack of selectivity, slow response time, expensive equipment, requiring a substantial amount of solvents, limited stability/selectivity, and time-consuming sample preparations. In contrast, among all the different types of analytical techniques, the fluorescence method is considered to be one of the most effective analytical techniques due to its rapid detection, ease of use, simplicity, low cost, and high sensitivity compared to all of the aforementioned processes, which enables a broader application in environmental monitoring, biological research, and disease diagnosis.[6,7] Hu *et al.* reported determination of riboflavin in urine and beverages by capillary electrophoresis with in-column optical fiber laser-induced fluorescence detection.[8] Zandomeneghi *et al.* demonstrated direct fluorometric determination of vitamin B$_2$ levels in low riboflavin-containing powders such as wheat flour.[9] Primarily RF is an electron carrier group and has a tendency to interact with an electron donor moiety and FRET is the primary mechanism for sensing. The current method for RF detection is based on FRET and is shown to be superior to

the methods stated above, such as a quicker response time, greater simplicity, lower cost, and more sensitivity and selectivity.[1] The majority of the biological processes occur *via* the fluorescence resonance energy transfer (FRET) mechanism, which is a non-radiative photophysical phenomenon comprising a donor and acceptor fluorophore separated by around 1–10 nm.[10] The excited state donor molecule emits energy and transfers it to the ground state acceptor molecule. As a result, dipole–dipole interactions between the donor and acceptor fluorophores cause overlap between the emission spectrum of the donor and the absorption spectrum of the acceptor. These unique attributes of the FRET principles promote their widespread use in a variety of fields, such as analytical science, biophysical studies, and the study of the conformational arrangement and dynamics of biomolecules like DNA, protein, *etc.*[10] However, FRET reports on carbon quantum dots are scarce in nature. Nowadays, CQDs are used as fluorescent biosensor materials for recognizing targeted analytes and for specifically detecting biologically active molecules *via* the FRET mechanism.[11,12] In the modern era, CQDs have emerged as a promising star in the category of zero-dimensional nanomaterials because of their outstanding sensitivity, rapid response time, relatively non-toxic nature, simple synthesis methods, low cost, chemical inertness, ease of functionalization, and many other advantages.[13,14] CQDs have superior properties compared to other semiconductor quantum dots, including high photostability against photobleaching and blinking, biocompatibility, and low toxicity.[15,16] CQDs exhibit intrinsic fluorescence properties due to their small size (1–10 nm), quantum confinement effect, monodisperse nature, presence of hetero-atom-based functional groups on the surface, *etc.*[17,18] Microwave-assisted synthesis of CQDs is significantly simpler, has a shorter reaction time, and avoids typical harsh reaction conditions involving the usage of strong acids/bases, high temperature, and prolonged reaction times. Recently, cutting-edge research has focused on the utilization of a simple and fast microwave treatment technique to produce CQDs from a variety of chemical and biomass precursors.[19] Biomass-derived CQDs have recently become a new frontier in the field of environmental science because of their high carbon content, eco-friendliness, straightforward methodology, cost-effectiveness, high quantum yield (QY), self-passivation, abundance, practicability, non-toxicity, sustainability, and recyclable nature. However, getting a suitable green resource to produce CQDs remains a challenging task.[20] The numerous precursors of biomass include plant leaves, fruit peels and juice, kitchen waste, agricultural waste, *etc.* The quantum yield of CQDs

derived from biomass waste precursors was found to be higher than that from chemical precursors.[21,22] Kundu et al. reported the synthesis of fluorescent CQDs using biomass precursor rice husk for selective and sensitive detection of Fe^{3+} and fluoroquinolones.[23] Monte-Filho et al. reported highly fluorescent CQDs from lemon and onion juices for determination of riboflavin in multivitamin/mineral supplements.[3] Lee and coworkers successfully transformed kiwi fruit peels into valuable kiwi fruit peel carbon dots (KFP-CDs) using a simple hydrothermal carbonization process. Without the need for any capping or passivation agents, KFP-CDs were employed as fluorescent ink for writing and drawing that was immediately visible when exposed to UV light. The findings suggest that KFP-CDs can be used as a cell labeling agent for mesenchymal stem cells, breast cancer, and thyroid cancer cells during in vitro imaging.[24] Atchudan et al. reported a simple hydrothermal approach to manufacture hydrophilic nitrogen-doped carbon dots (HN-CDs) from dwarf banana peel biowaste that selectively and sensitively detect Fe^{3+} ions by the FL quenching of HN-CDs.[25] Atchudan et al. employed a one-pot hydrothermal carbonization method to synthesize bright fluorescence nitrogen-doped carbon dots (NCDs) using Piper betel (Betel) leaf. The fluorometric method was used to determine the Fe^{3+} ion with a detection limit of 0.43 mM due to the resonance energy/electron transfer (RET) mechanism.[26] A one-step hydrothermal approach is employed by Atchudan et al. to produce extremely durable fluorescent nitrogen-doped carbon dots (FNCDs) using Phyllanthus acidus and aqueous ammonia. With a detection limit of 0.9 μM, they are utilized here for the label-free, sensitive, and selective detection of Fe^{3+}.[27] Atchudan et al. reported an effective hydrothermal synthesis of N-CDs using aqueous ammonia as the nitrogen source and unripe peach fruit. The synthesised N-CDs have good catalytic activity in an alkaline solution and are extremely biocompatible, thus can be employed as fluorescent imaging probes.[28]

Medicinal plants are a unique gift to humanity that promote a disease-free and healthy existence. Phyllanthus emblica, often known as the Indian gooseberry, has great significance in Ayurveda and is commonly used as medicine in liver tonic, antipyretic, ulcer prevention, common cold, hair tonic, etc. It contains a lot of minerals including sodium, calcium, iron, phosphorus, and plenty of polyphenols, tannins, alkaloids, cholesterol, carotene and amino acids. It is a good source of vitamin C (200–900 mg per 100 g of the consumable component) and has various chemical elements with biological action.[29,30] Arul et al. reported the synthesis of CQDs from Indian gooseberry using a hydrothermal method involving ammonia as a doping agent and studied their catalytic ability in the detoxification of textile effluents.[31] Atchudan et al. demonstrated hydrothermal synthesis of nitrogen-doped carbon dots using ammonium hydroxide as a doping agent and applied them as a promising staining agent on human colon cancer cells by cellular imaging.[32] All the synthetic protocols have certain limitations as they involve high temperature (200 °C), use of chemical reagents for doping and long reaction time (12 h).[31,32]

Herein, we report a simple, rapid, low-cost, one-step microwave-assisted carbonization technique to synthesize highly fluorescent N-CQDs from Phyllanthus emblica (Indian gooseberry) as the biomass precursor. To the best of our knowledge, this is the first report in which without using any harsh chemicals, intrinsic nitrogen-containing N-CQDs were developed. The synthetic protocol involved a purely green methodology. The presence of ascorbic acid, citric acid, polyphenols, and amino acids is responsible for the nitrogen source in Indian gooseberry, which results in surface passivation by the bottom-up methodology in the presence of microwave irradiation (10 min) to form N-CQDs. The synthesized N-CQDs showed high selectivity for detection of riboflavin and the interaction was confirmed by the FRET mechanism. The limit of detection was found to be in the nanomolar range. Moreover, the as-prepared nanoprobe was validated in real samples (vitamin B$_2$ supplements).

2. Experimental section

2.1. Materials

For the preparation of fluorescent N-CQDs, fresh Indian gooseberries were bought from the local market of Patiala, Punjab. Sodium phosphate monobasic, sodium citrate, Trizma base, 4-(2-hydroxyethyl)-1-piperazineethanesulfonic acid (HEPES), sodium chloride, riboflavin, alanine (Ala), arginine (Arg), asparagine (Asn), aspartic acid (Asp), cysteine (Cys), glutamic acid (Glu), glutamine (Gln), histidine (His), isoleucine (Ile), leucine (Leu), lysine (Lys), methionine (Met), threonine (Thr), tryptophan (Trp), tyrosine (Tyr), valine (Val), and N-acetyl-L-cysteine methyl ester were purchased from Sigma-Aldrich, India and were used as such without any further purification. Ascorbic acid (AA), glucose, and dopamine were purchased from HiMedia and used as obtained. Quinine sulfate was purchased from Loba Chemie and was used as a standard for photoluminescence quantum yield (PLQY) measurements. Double-distilled water has been used throughout this investigation. The pH of the buffers was adjusted to a final value of (±0.02) using a pH meter (EUTECH pH/Ion 510) at ∼24–25 °C. The 0.22 μM and 0.02 μM membrane filters were obtained from Merck Millipore and Whatman (GE Healthcare Life Sciences), respectively. The dialysis membrane (dialysis membrane-110 LA395-1MT) having a molecular weight cut off between 12 and 14 kDa was obtained from HiMedia Laboratories, India. For real sample testing, a commercially available multivitamin/multimineral (vitamin B$_2$) supplement was purchased from medical stores in Patiala, Punjab.

2.2. Synthesis of N-CQDs

A microwave-assisted synthesis method was used to synthesize N-CQDs. The gooseberries were washed in double-distilled water, cut into small pieces, and transferred into a mixer grinder followed by grinding for ∼10 minutes till they were fully crushed. The resulting juice was extracted using a sieve and filtered with Whatman® filter paper. The filtrate (juice) was transferred into a microwave vial and the reaction was set up in
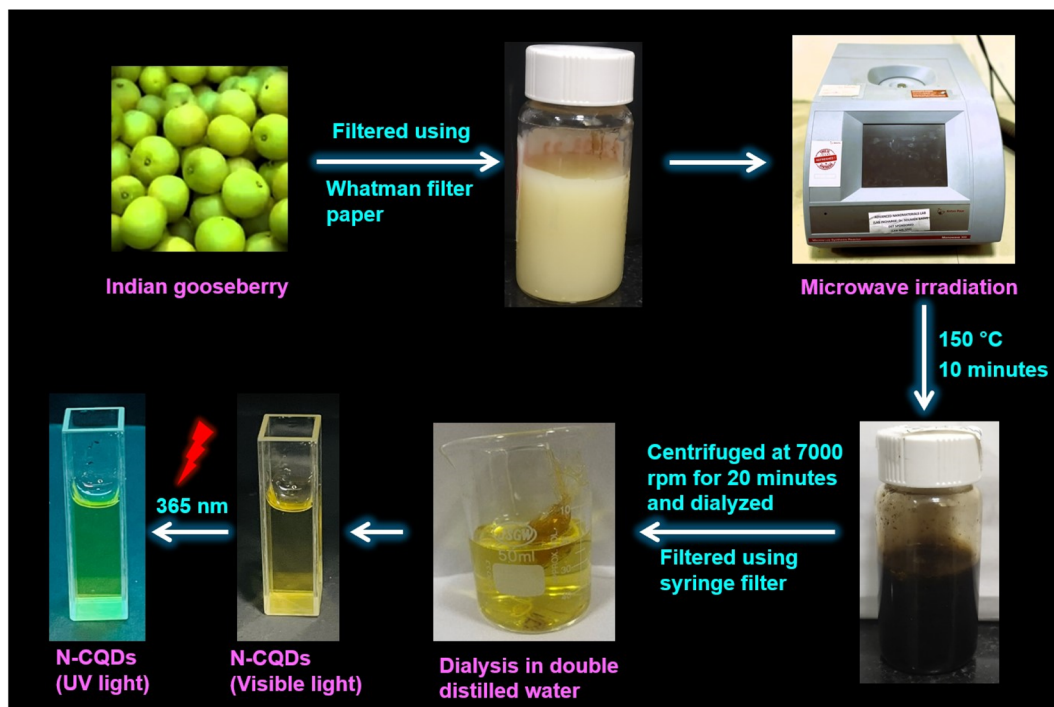
Scheme 1 Schematic representation of the synthetic protocol of N–CQDs from Indian gooseberry.

a microwave synthesizer (Anton Parr) at 150 °C for 10 minutes. Carbonization caused a change in the juice color from pale green to dark brown indicating the formation of N-CQDs. After cooling down the solution to room temperature, it was centrifuged at 7000 rpm for 20 minutes, and the solution was decanted. The decanted solution was transferred into a dialysis bag whereby it was dialyzed against double-distilled water for three days (at ~24–25 °C without stirring). The clear light brown color solution was filtered further through a 0.22 µm syringe filter followed by a 0.02 µm membrane filter, respectively to remove the larger particles. The schematic representation of the protocol involving the synthesis of N-CQDs is shown here (Scheme 1). Finally, the clear light brown solution of N-CQDs was collected, and stored in a refrigerator at 4 °C for further experimental studies.

2.3. Characterization of N-CQDs

2.3.1. Electron microscopy. The synthesized N-CQDs were characterized by high-resolution transmission electron microscopy (HRTEM) on JEM 2100 plus (JEOL) fitted with a charge-coupled device (CCD) camera at an acceleration voltage of 80–200 kV. The samples were prepared by spreading a small droplet of diluted N-CQDs solution (1 : 1 (v/v) of N-CQDs and water) on a copper grid and allowed to dry at room temperature (~24–25 °C) overnight for ~12–16 hours.

2.3.2. X-ray photoelectron spectroscopy (XPS) and energy dispersive spectroscopy (EDS). The XPS of N-CQDs was performed on a Physical electronics PHI 5000 Versa Probe III. The spectra were first baseline corrected and then the peaks were identified by the peak analyzer option and deconvoluted using

multiple peak-fitting involving the Gaussian function available in the OriginPro 2021 software. Table S1† depicts various parameters obtained during the deconvolution of the XPS data and the deconvoluted peaks were best fit using $R^2 = 0.99$. The EDS of N-CQDs was recorded using a Talos F200S (Thermo Fisher Scientific).

2.3.3. Grazing-incidence X-ray diffraction (GIXRD). The diffraction pattern of N-CQDs was recorded on a Rigaku SmartLab in the angular range (2θ) of 10–90°. The scan resolution was 0.0001° with a scan speed of 3.02° min^{-1}.

2.3.4. Raman spectroscopy. The purity and structural defects of the N-CQDs were evaluated using a LabRAM HR Confocal Micro-Raman Spectrometer, (HORIBA, France) using a 532 nm laser as an excitation source that was focused onto the sample spot using a 50× objective lens. A charge-coupled device (CCD) multichannel array detector was used to detect the signal. The Rayleigh scattering was eliminated by collecting the scattered light *via* the same objective and allowing it to pass through a 532 nm edge filter. All the spectra were collected in the range of 400–2000 cm^{-1} and the final spectrum was averaged over 2 scans with a resolution of ~1 cm^{-1}. The data were acquired using LabSpec 6 software provided with the Raman spectrometer and replotted using OriginPro 2021. For XPS, EDS, XRD, and laser Raman spectroscopy, samples of N-CQDs (without any dilution) were drop cast on a glass coverslip to form a thin film and allowed to dry at room temperature (~24–25 °C) overnight for ~12–16 hours.

2.3.5. Attenuated total reflectance Fourier-transform IR (ATR FT-IR) spectroscopy. An IRTracer-100 spectrophotometer (Shimadzu), comprising the QATR™ single-reflection integration-type ATR accessory involving a diamond crystal

and an air-cooled DLATGS detector, was used to obtain the ATR-FTIR spectra of the N-CQDs. A sample drop of 10 μL was used for recording the spectra in the range of 400–4000 cm^{-1}. All the spectra were recorded at a resolution of 2 cm^{-1} in the transmittance mode. The final spectrum was an average of 100 scans. The crystal surface was cleaned with methanol before putting a sample drop and the background scan was run with 100 accumulations prior to recording the spectrum. OriginPro 2021 was used for replotting the spectral data.

2.3.6. UV-visible spectroscopy and zeta potential (ζ) measurements. The UV-vis absorption spectra of aqueous solutions of N-CQDs were recorded on a UV-vis spectrophotometer (Shimadzu, RF-2600) using a quartz cuvette of 1 cm path length. 100 μL of the N-CQD solution was added into double-distilled water to a total volume of 3 mL for recording the absorbance. The zeta potential experiments of N-CQDs were carried out on a Zetasizer 2000, nano series-ZS (Malvern Instruments Ltd, UK).

2.3.7. Preparation of N-CQD samples for fluorescence studies. 50 μL of the synthesized N-CQDs was added to 2.45 mL of double-distilled water to make a total volume of 2.5 mL. The volume of N-CQDs was kept constant while the concentration of riboflavin (RF) was varied (0–2.2 μM) during the fluorescence emission measurements with an excitation wavelength of 340 nm.

2.3.8. Steady state fluorescence spectroscopy. The fluorescence spectra of N-CQDs were collected using a Shimadzu RF-6000 spectrofluorometer. The following parameters were used for collecting the fluorescence spectra of N-CQDs: $\lambda_{ex} = 340$ nm with a scan range of 350–650 nm (in aqueous medium) and $\lambda_{ex} = 360$ nm with a scan range of 370–700 nm (at pH 7.4). The excitation and emission bandwidths were varied for different sets of fluorescence studies involving N-CQDs. For collection of the excitation wavelength-dependent emission spectra and for volume optimization studies in aqueous medium and pH 7.4, both excitation and emission bandwidths were set at 10 nm. Similarly, for N-CQD optimization studies (i.e. for optimizing N-CQD storage duration, and optimal fluorescence emission as a function of pH), both the bandwidths were fixed at 5 nm whereas for optimizing the reaction duration in the microwave synthesizer and for biomolecule sensing studies, the excitation and emission bandwidths were set at 5 and 10 nm, respectively. Further to estimate the limit of detection, binding constant, and Stern–Volmer quenching constant (K_{sv}), the emission intensities were fitted using a linear equation available in the Origin-Pro 2021 as shown below:

$$y = a + bx \qquad (1)$$

y is the ratio of fluorescence intensities i.e. F_0/F where parameters 'F_0' and 'F' indicate the fluorescence intensity in the absence and presence of RF, respectively. 'a' is the intercept, 'b' is the slope, and 'x' represents quencher concentration (vitamin B$_2$). All of the steady state fluorescence experiments were performed at least three times.

2.3.9. Photoluminescence quantum yield (PLQY) measurements. The photoluminescence quantum yield (PLQY)

of N-CQDs was measured using quinine sulfate in 0.1 M H$_2$SO$_4$ as a standard reference solution (quantum yield 0.546).[10] The PLQY values were calculated using the following equation:[34]

$$\phi_S = \phi_R \times \frac{A_S}{A_R} \times \frac{(Abs)_R}{(Abs)_S} \times \frac{\eta_S^2}{\eta_R^2} \qquad (2)$$

The parameters 'ϕ_S' and 'ϕ_R' represent the fluorescence quantum yield of the sample (N-CQDs) and the reference solution (quinine sulfate), respectively. 'Abs' denotes absorbance, 'A' represents the area under the fluorescence emission peak, and 'η' is the refractive index of the solvent (1.333 for water). The subscripts 'S' and 'R' denote the corresponding parameters for the N-CQDs (sample) and quinine sulfate (reference), respectively.

2.3.10. Time-resolved fluorescence spectroscopy. Time-resolved fluorescence emission decays were recorded with a time correlated single photon counting (TCSPC) fluorometer instrument using a modular fluorescence lifetime system (DeltaFlex, HORIBA Scientific) with an excitation source of 340 nm (nano-LED pulse diode). The instrument response function (IRF) was recorded using LUDOX®TMA colloidal silica and 34 wt% suspension in distilled water (Sigma-Aldrich), and the full-width at half-maximum (FWHM) was estimated to be ~200 ps. For fluorescence lifetime measurements, the emission polarizer was set at the magic angle (54.7°) with respect to the excitation polarization. An emission monochromator was fixed at 430 nm with a bandpass of 16 nm. The time-resolved lifetime measurements were carried out w.r.t. 100 ns decay range and the time per channel is 0.055 ns. A long-pass filter was placed just after the sample to block any scattering from the sample. All of the decays were acquired at 25 °C and replotted using OriginPro 2021. The fluorescence emission decays were further deconvoluted with respect to the instrument response function and were analyzed and fitted using the following equation:[10]

$$I(t) = \sum_i \alpha_i \, e^{-\frac{t}{\tau_i}} \qquad (3)$$

where α_i and τ_i represent the contributions and lifetimes, respectively, of the different lifetime components, and $I(t)$ represents the fluorescence intensity at time t. All the data were acquired at 25 °C.

3. Results and discussion

3.1. Morphological characterization and compositional analyses of N-CQDs

The size and morphological characteristics of N-CQDs were confirmed by HR-TEM. Fig. 1a and S1a† show that the N-CQDs are spherical particles which are also monodisperse. The histogram plot (Fig. 1a inset) depicted that the average diameter of N-CQDs was 8.1 nm with the particle size ranging from 2 to 16 nm, which closely resembles the Gaussian distribution. Fig. 1b shows the X-ray diffraction pattern of synthesized N-CQDs. An intense broad diffraction peak was observed around $2\theta = 24.5°$ for the (002) lattice plane, and a weak spike appeared at $2\theta = 42.9°$ for the (100) lattice plane, demonstrating an
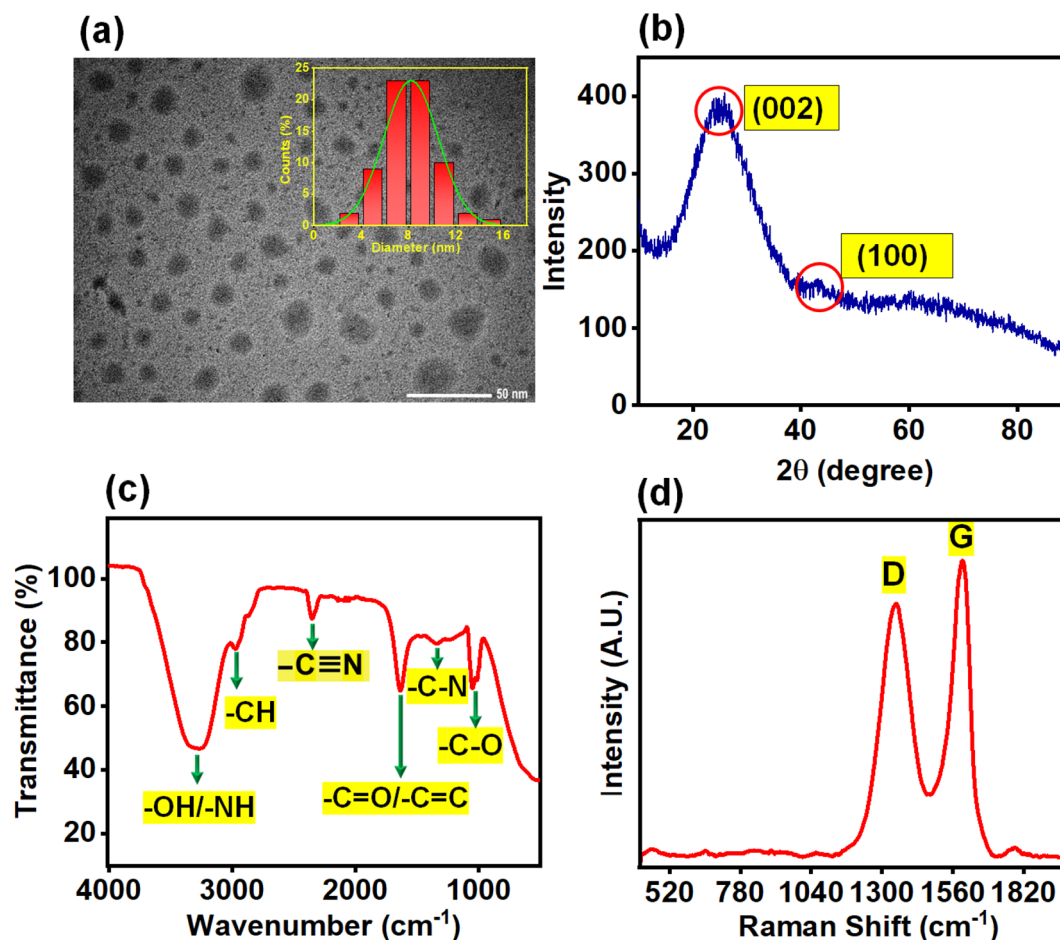
Fig. 1 (a) HR-TEM image of N-CQDs, inset representing the particle size distribution histogram plot, (b) XRD spectrum, (c) FTIR spectrum and (d) Raman spectrum of N-CQDs.

amorphous carbon phase and a partial graphitization of the N-CQDs, respectively which is in good accord with other literature reports.[33,34] The partial graphitization is due to the presence of nitrogen and oxygen-containing moieties on the surface of N-CQDs.[30,31]

The interlayer distance (*d*-spacing) was determined using Bragg's equation:

$$n\lambda = 2d\sin\theta \qquad (4)$$

where 'λ' denotes the wavelength of the incident X-ray (λ = 1.5406 Å), 'n' is a positive integer that signifies the "order" of reflection, and 'd' is the variable that indicates the spacing between the diffracting planes. The estimated *d*-spacing values of N-CQDs were 0.36 and 0.21 nm, which correspond to (002) and (100) lattice planes, respectively. The different interlayer distances of N-CQDs, compared to bulk graphite (0.34 nm), suggest that nitrogen and oxygen-containing functional groups are well decorated on the surface of N-CQDs.[32,35,36] FTIR spectral analysis of as-prepared N-CQDs (Fig. 1c) aided in identifying the functional groups attached to the surface. The broad peak at 3364–3224 cm^{-1} was recognized as the stretching vibration of the O–H/N–H band, whereby hydrogen bonding is responsible

for its broadening,[37] the weak band found at 2970 cm^{-1} was attributed to stretching vibrations of the C–H band, and the signal at 2355 cm^{-1} was ascribed to –C≡N stretching vibration.[38] The signal at 1633 cm^{-1} was assigned to stretching vibrations of alkenyl C=C/carbonyl C=O[39] groups present in N-CQDs. The peaks centered at 1366 cm^{-1} and 1028 cm^{-1} were ascribed to –C–N stretching,[40] and –C–O stretching[41] respectively. Thus, the FTIR spectra corroborated successful incorporation of the amino, hydroxyl, and carboxyl groups on the surface, conferring high polarity and water solubility of the N-CQDs. Fig. 1d shows the Raman spectrum of N-CQDs, comprising two peaks at 1378 cm^{-1} and 1598 cm^{-1}, which are attributed to the D-band and G-band, respectively.[42,43] The D-band appears due to the breathing motion of κ-point phonons with the A_{1g} symmetry, which is induced by defects in the sp^3 carbons, whereas the G-band occurs due to the first-order scattering of E_{2g} phonons in sp^2 hybridized carbon atoms.[42,43] Therefore, overall, the Raman data demonstrated that sp^3 (D-band) and sp^2 (G-band) hybridized carbon defects were present in N-CQDs. Furthermore, the intensity ratio of the D to G band (I_D/I_G) is 0.85 demonstrating that N-CQDs possess a moderate degree of graphitization.[44]

X-ray photoelectron spectroscopy (XPS) is the most useful tool for elemental identification as well as to determine the surface oxidation state and the exact quantity (percentage) of the elements present. The deconvoluted XPS spectra for the C 1s, N 1s, and O 1s elements are shown in Fig. 2, together with the survey spectrum of the synthesized N-CQDs. The elemental carbon (64.9%), nitrogen (4.1%), and oxygen (31.1%) peaks emerged at 283.1, 397.8, and 531.3 eV, respectively (Fig. 2a).[33,45,46] The deconvolution spectrum of O 1s showed one binding energy peak at 531.8 eV, corresponding to the –C=O/–C–O–C groups (Fig. 2b and Table S1†).[47] The deconvolution spectrum of N 1s displayed two peaks at 399.3 and 401.1 eV, owing to amide –C$_3$N (pyridine N) and –C–N–C (pyrrolic N) groups on the N-CQD surface, respectively (Fig. 2c and Table S1†).[39] The C 1s deconvolution spectrum exhibits characteristic peaks at 283.8, 285.3 and 287.2 which are attributed to transitions involving the –C=C/–C–C, –C=N/–C=O, and –O–C=O, respectively (Fig. 2d and Table S1†).[48,49] The primary peak

around 284.5 eV corresponds to the carbon atoms in the graphitic structure. This peak clearly shows that the carbon dots synthesized have mostly sp^2 carbons.[50,51] The XPS results corroborated well with the previous findings of FTIR analysis. In addition, the presence of C, N, and O elements in the N-CQDs was also confirmed by energy dispersive X-ray spectroscopy (EDS) as shown in Fig. S1b.†

3.2. Optical properties of N-CQDs

The absorption spectrum of N-CQDs showed a peak at 280 nm along with a long tail at approx. 355 nm (Fig. 3a). The absorption maximum at 280 nm was attributed to the π–π* transition of the conjugated C=C (sp^2) bonds[54] whereas the band at 355 nm corresponded to the n–π* transition of the C=N/C=O/ N=O groups (containing heteroatoms of nitrogen and oxygen) present on the surface of N-CQDs.[55] The presence of heteroatom-containing functional groups was also confirmed by XPS, EDS, and FTIR analysis as already mentioned previously
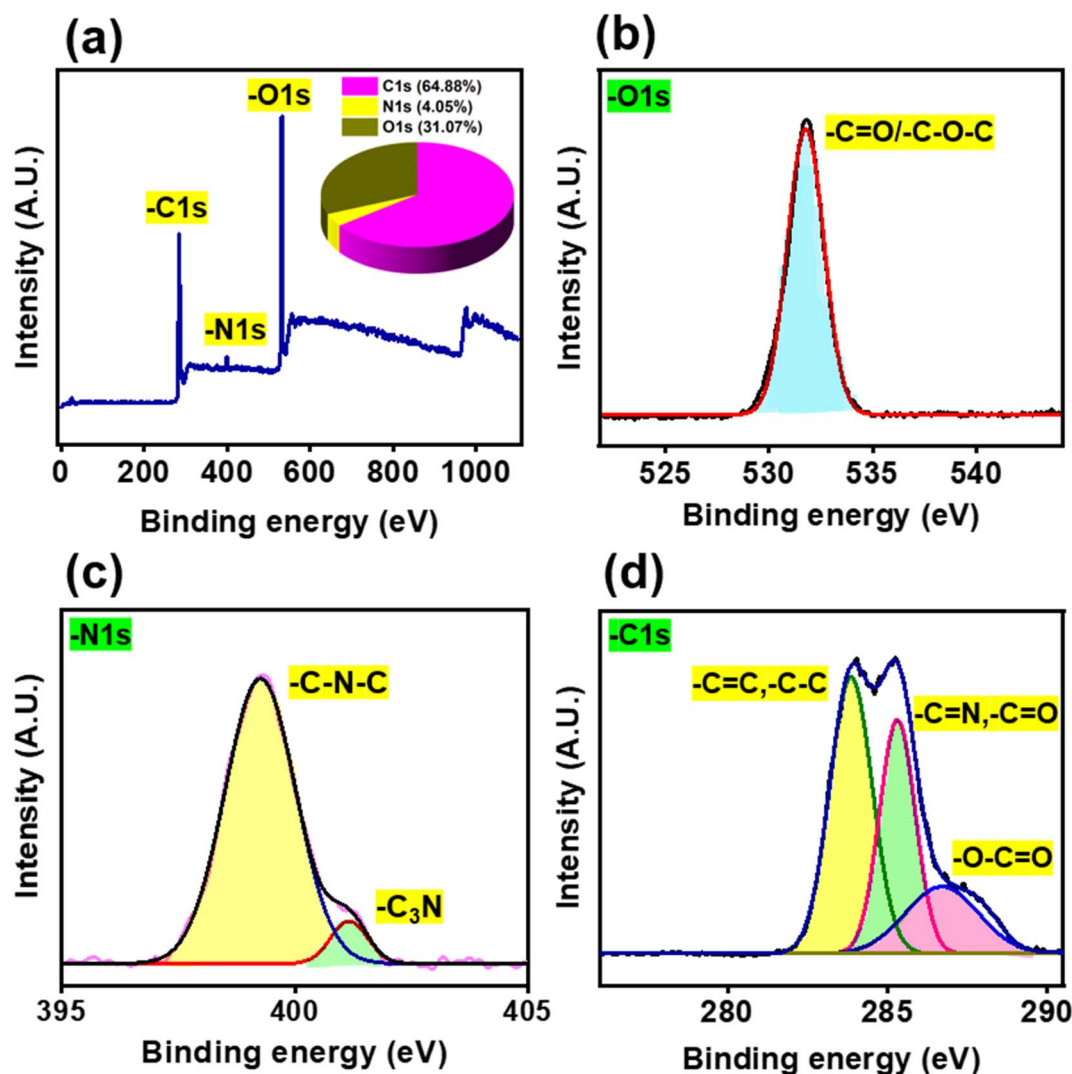

Fig. 2 (a) XPS survey spectrum of N-CQDs and (b–d) deconvoluted XPS spectra of N-CQDs represented in an element-specific manner viz. (b) O 1s, (c) N 1s, and (d) C 1s.
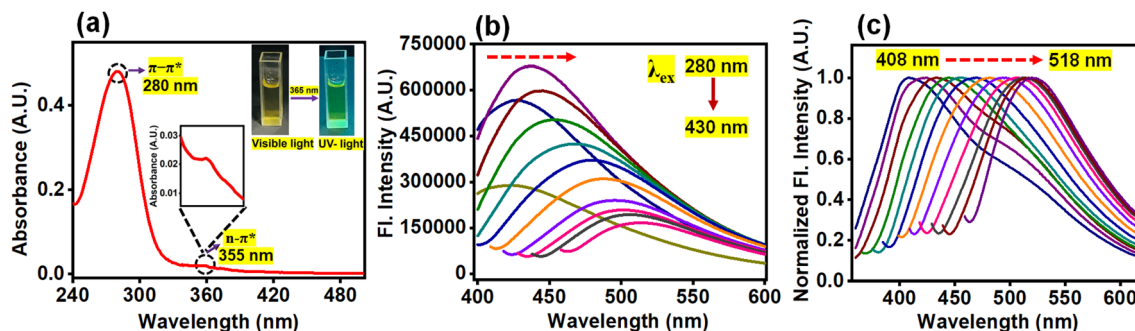
Fig. 3 (a) UV-visible absorption spectrum of N-CQDs with the inset picture representing N-CQDs under visible and UV light illumination. The other inset image depicts the magnified representation of the 355 nm band. Excitation wavelength-dependent (b) changes in fluorescence emission spectra of N-CQDs and (c) peak position-normalized fluorescence emission of N-CQDs clearly depicting the spectral shift, indicated by a dashed red arrow, from 408 nm to 518 nm in aqueous medium (λ_{ex}: 280 nm to 430 nm).

(Section 3.1). The inset of Fig. 3a shows that N-CQDs exhibit a light brown color as observed by the naked eye and green fluorescence emission under UV light illumination at 365 nm. The fluorescence emission of N-CQDs is due to photoinduced charge separation along with entrapment at the surface, which causes radiative recombination between hole and electron pairs.[56] In an aqueous medium, N-CQDs showed a maximum emission intensity at 430 nm upon excitation at 340 nm (Fig. 3b); while in HEPES buffer (pH 7.4), the emission maximum appeared at 450 nm upon excitation at 360 nm (Fig. S2†). In both aqueous and buffer media, excitation wavelength-dependent emission spectral shifts were observed. The excitation-dependent emission properties of N-CQDs are due to the quantum confinement effect, surface defects, zigzag sites, formation of the aromatic structure on their surface, non-uniform particle distribution, *etc.*[57] Fig. 3c and S2b† display normalized fluorescence emission of N-CQDs in aqueous and buffer media, respectively. In aqueous medium, N-CQDs showed a significant bathochromic shift (∼110 nm) in the fluorescence emission when the excitation wavelength was varied from 280 to 430 nm (Fig. 3b and c). Similarly, in HEPES buffer, a bathochromic shift of ∼116 nm was observed upon varying the excitation wavelengths in a similar range (Fig. S2†). This experimental study reveals that N-CQDs showed similar kinds of excitation-dependent emission properties irrespective of the dispersant medium. Moreover, these photophysical studies of the as-prepared nanoprobe in a buffer medium reaffirm that N-CQDs can be used as an effective nanosensor under physiological conditions.

3.3. Optimization of N-CQDs

As aforementioned (Section 3.2), the synthesized N-CQDs exhibited photoluminescence (PL) upon irradiation with UV light. In order to develop an effective optical nanosensor with strong PL properties, it is essential to optimize the reaction time, volume, and time duration of storage of the as-prepared N-CQDs.

3.3.1. Reaction time and volume optimization. It is well known that the reaction time affects the photoluminescence characteristics of N-CQDs. To figure out the optimum reaction

conditions, N-CQDs were synthesized by varying the reaction times ranging from 5 minutes to 20 minutes. We observed that our microwave pyrolysis method, involving a reaction time of 10 minutes at 150 °C, yields the desired N-CQDs with the highest PL intensity (Fig. 4a).

After three days of dialysis, the synthesized N-CQDs were dispersed in aqueous solution using double-distilled water followed by centrifugation and filtration. We noticed that N-CQDs were highly water soluble. Further, for the sensing efficiency as well as to achieve the maximum fluorescence intensity of the synthesized nanoprobe, volume optimization is required. So next for volume optimization, we monitored the changes in the N-CQD emission intensity by adding varying amounts of aliquots (10–100 μL), from the respective stock solution of N-CQDs, into double-distilled water. It was found that 50 μL of N-CQDs and 2.45 mL of double-distilled water exhibited the maximum PL intensity (Fig. 4b).

3.3.2. Storage duration optimization. The emission spectra of N-CQDs were recorded at various time intervals for up to 60 days (*i.e.* ∼2 months). Fig. 4c shows the emission spectra of N-CQDs at different storage durations, which clearly depicted no appreciable changes in the fluorescence intensity. Therefore, the findings clearly indicated that the synthesized nanoprobe was highly stable in an aqueous medium for prolonged time and hence, could be useful for diverse analytical applications.

3.4. Stability of N-CQDs

The photostability and chemical stability of an ideal nanosensor are essential for its practical applications. Therefore, to examine the stability of N-CQDs, the effects of photoirradiation, ionic strengths, and pH were investigated. The inherent pH value of N-CQDs was found to be ∼3.2, implying its acidic nature, presumably due to the presence of carboxylates. Furthermore, the zeta potential value (−4.37 mV) of N-CQDs confirmed the presence of negatively charged moieties on the N-CQD surface (Fig. S3a†), which corroborated with the inherent pH value of the as-prepared nanoprobe (due to the presence of carboxylates). Additionally, N-CQDs showed remarkable stability in the pH range of 3 to 7 with minute changes in fluorescence emission intensity as well as their
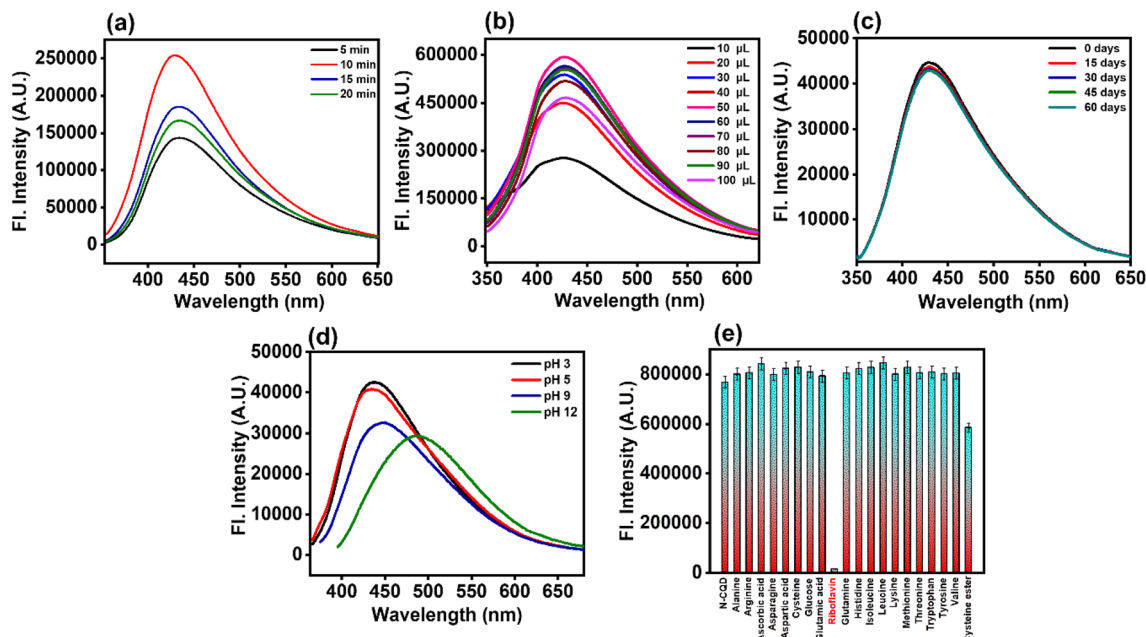
Fig. 4 Fluorescence emission spectra of N-CQDs by optimizing the (a) reaction time, (b) volume ratio, (c) storage time, and (d) variable solution pH. (e) Selectivity studies of N-CQDs with different amino acids and bioactive molecules. All the experiments were performed in aqueous medium.

emission maxima (Fig. 4d). Moreover, the fluorescence intensity of N-CQDs was also recorded in HEPES buffer at pH 7.4, which also confirmed that the synthesized nanoprobe was significantly stable and can be effectively used in physiological pH (Fig. S3b†). Thus, the synthesized N-CQDs can be efficiently applied as a versatile pH sensor in the pH range of pH 3 to 7.4. In the acidic to neutral pH range, several functional groups present on the surface of the N-CQDs lead to higher net surface charge (negative), which in turn leads to electrostatic repulsion and enhances the PL emission.[41] Nevertheless, as the alkalinity of the solution was increased, a drop in the PL intensity was observed. This is most likely to be caused by deprotonated carboxylates present on the surface. Additionally, at higher alkaline pH, the charged polyphenols get deprotonated coupled with deprotonation of ammonium ions. These deprotonated species may further trigger negative charge accumulation. Consequently, energy levels are being occupied, and the electronic transitions of different emissive traps are being hindered which leads to a drop in PL emission along with bathochromic shift in the emission spectra. Thus, there is a positive correlation between acidic and basic ranges implying the practical usability of N-CQDs as a pH sensor.[52,53] Furthermore, the influence of ionic strength on N-CQD emission was evaluated in the presence of 0–2 M NaCl solution. No appreciable changes in the PL intensity along with the emission maxima of N-CQDs were observed by varying the ionic strength of the medium, clearly suggesting high stability of the nanoprobe in the presence of a salt (Fig. S3c†). Additionally, the PL intensity of N-CQDs remained stable upon continuous photo-irradiation with a xenon-arc lamp of 150 W as shown in Fig. S3d.† Moreover, we found that our N-CQDs can be used as fluorescent ink

which shows green emission (Fig. S3d† inset) upon irradiation with UV light (365 nm), indicating its potential utility in practical applications.

3.5. Selectivity studies of N-CQDs

Selectivity analysis is one of the most important factors for the development of a novel nanosensor. In order to verify the selectivity of the analytical sensing platform, the changes in fluorescence intensity of N-CQDs were monitored in the presence of several bioactive molecules and amino acids. A particular concentration of different amino acids (1 mM) such as alanine (Ala), arginine (Arg), asparagine (Asn), aspartic acid (Asp), cysteine (Cys), glutamic acid (Glu), glutamine (Gln), histidine (His), isoleucine (Ile), leucine (Leu), lysine (Lys), methionine (Met), threonine (Thr), tryptophan (Trp), tyrosine (Tyr), and valine (Val), in addition to several other bioactive molecules such as N-acetyl-L-cysteine methyl ester, ascorbic acid (AA), glucose, and riboflavin (RF *i.e.* vitamin B₂) (13.25 μM) was prepared. Fig. 4e reveals that riboflavin (RF) showed maximum fluorescence quenching of the N-CQDs, whereas the PL intensity of the N-CQDs upon addition of the remaining analytes remained almost unchanged. Thus, our N-CQDs as a nanosensor were found to be extremely selective towards the detection of RF. Therefore, it can be concluded that N-CQDs have excellent practical usability as fluorescent nanosensors for specific detection of RF *i.e.* vitamin B₂.

3.6. Determination of photophysical parameters

As we demonstrated earlier, N-CQDs exhibit excellent fluorescence. Therefore, to further decipher their photophysical

Table 1 Photophysical parameters of N-CQDs in the presence of RF[a]

System	ϕ	$\tau_m{}^b$ (ns)	k_r (ns^{-1})	k_{nr} (ns^{-1})	k_{ET} (ns^{-1})
N-CQDs (aqueous medium)	0.48	2.26	0.21	0.23	—
N-CQDs (aqueous medium) + RF	0.19	1.55	0.08	0.36	0.20

[a] Error limit = ±5%. [b] $\tau_m = \alpha_1\tau_1 + \alpha_2\tau_2 + \alpha_3\tau_3$.

properties, there is a need to calculate the photoluminescence quantum yield (PLQY). Using eqn (2), the PLQY of N-CQDs was estimated to be ~48%, which reaffirmed that the as-prepared nanoprobe is a bright fluorophore. However, in the presence of RF, the PLQY of N-CQDs was significantly reduced to ~19%, confirming a remarkable quenching of its fluorescence (Table 1). The fluorescence quenching phenomenon was also supported by TCSPC analysis. The addition of RF resulted in a decrease in the mean fluorescence lifetime of N-CQDs (Table 1).

From the PLQY (ϕ) and mean lifetime (τ_m) data, fluorescence lifetime (τ_f), and different radiative (k_r) and non-radiative (k_{nr}) rate constants, were estimated using the following equations:[10]

$$k_r = \frac{\phi_f}{\tau_f} \tag{5}$$

$$\frac{1}{\tau_f} = k_r + k_{nr} \tag{6}$$

From Table 1, it is observed that 'k_r' values of N-CQDs reduced significantly, while 'k_{nr}' values enhanced in the presence of RF (vitamin B$_2$). Thus, these results strongly indicated that highly fluorescent N-CQDs turned to a less fluorescent complex in the presence of RF and presumably, the excited-state electron transfer process was responsible for quenching. In order to gain insights into the quenching mechanism of the as-prepared nanosensor in the presence of RF, different concentrations of RF (vitamin B$_2$) were added to N-CQDs and the changes in the fluorescence emission were recorded. We observed that the PL intensity of N-CQDs gradually quenched as a function of variable concentrations of RF at shorter emission wavelengths in aqueous and buffer media as well as in the presence of a real sample of vitamin B$_2$, as shown in Fig. 5a, S4a and b,† respectively. To comprehend the extent of quenching efficiency of N-CQDs, Stern–Volmer quenching constants were evaluated using the following equation:[10]

$$\frac{F_0}{F} = 1 + K_{SV}[Q] \tag{7}$$

Fig. S5† depicts a graph between F_0/F and Q i.e. concentration of the quencher (RF) in different media. The parameters 'F_0' and 'F' indicate the fluorescence intensity in the absence and presence of RF, respectively. 'K_{sv}' signifies the Stern–Volmer quenching constant, which was estimated from the slope of the plots in aqueous as well as in pH 7.4 buffer medium and real sample. The Stern–Volmer quenching constants of N-CQDs are

tabulated in Table 2 which indicate that the extent of quenching by vitamin B$_2$ remains the same irrespective of the medium. The values of R^2 were found close to unity, indicating the acceptable linearity of the developed nanosensor.

Further, to estimate the N-CQD-RF stoichiometry, and to understand the strength of interaction and binding between N-CQDs and RF (vitamin B$_2$), the excited-state binding constant was calculated (Table 2) by taking the corresponding fluorescence intensity into account and using the 1 : 1 linear Benesi–Hildebrand equation as follows:[58]

$$\frac{1}{F_0 - F} = \frac{1}{F_0 - F_1} + \frac{1}{K_1[RF](F_0 - F)} \tag{8}$$

'F_1' signifies the fluorescence intensity of the N-CQDs–RF complex. The plot of ($1/F_0 - F$) against 1/[RF] yields a straight line. From the reciprocal of the respective slope values, the binding constant (K_1) of the N-CQDs–RF complex was evaluated in an aqueous, physiological buffer medium and real samples of vitamin B$_2$ supplements, which are shown in Table 2 and in Fig. S6.† Overall, the binding constant (K_1) of N-CQDs and RF (vitamin B$_2$) appears to be similar irrespective of the source of vitamin B$_2$ and the dispersant medium. Moreover, the limit of detection of vitamin B$_2$ at physiological pH (isolated sample) and for real samples (pharmaceutical tablets) appears to be almost similar (Table 2) which, once again, reaffirms the suitability and efficiency of our nanosensor towards detection of vitamin B$_2$ in real samples.

3.7. Elucidation of the sensing mechanism of RF (vitamin B$_2$) using N-CQDs

It has been documented in the literature that the solution pH affects the structure of RF (vitamin B$_2$). The anionic species of RF at pH > 9.7 exhibits weak fluorescence while the neutral and cationic species of RF have considerable fluorescence properties with significant quantum yield.[59,60] Therefore, for our studies, sensing of RF was executed in neutral aqueous and buffer media by adjusting the solution pH and thereafter, we directed our efforts to delineate the mechanism of exclusive sensing of RF (vitamin B$_2$) by the N-CQDs. The subsequent titrations of N-CQDs were carried out by adding different concentrations of RF (0–2.2 µM) in aqueous solution (Fig. 5a), HEPES buffer medium at pH 7.4 (Fig. S4a†), and real samples of vitamin B$_2$ tablets (Fig. S4b†). At physiological pH (i.e. at pH 7.4), both N-CQDs (Fig. S3a†) and RF are negatively charged since the pI of the latter is 6[5] and hence, electrostatic interactions between these moieties are unlikely. However, as aforementioned, we observed that only the N-CQDs–RF signal produced a noteworthy
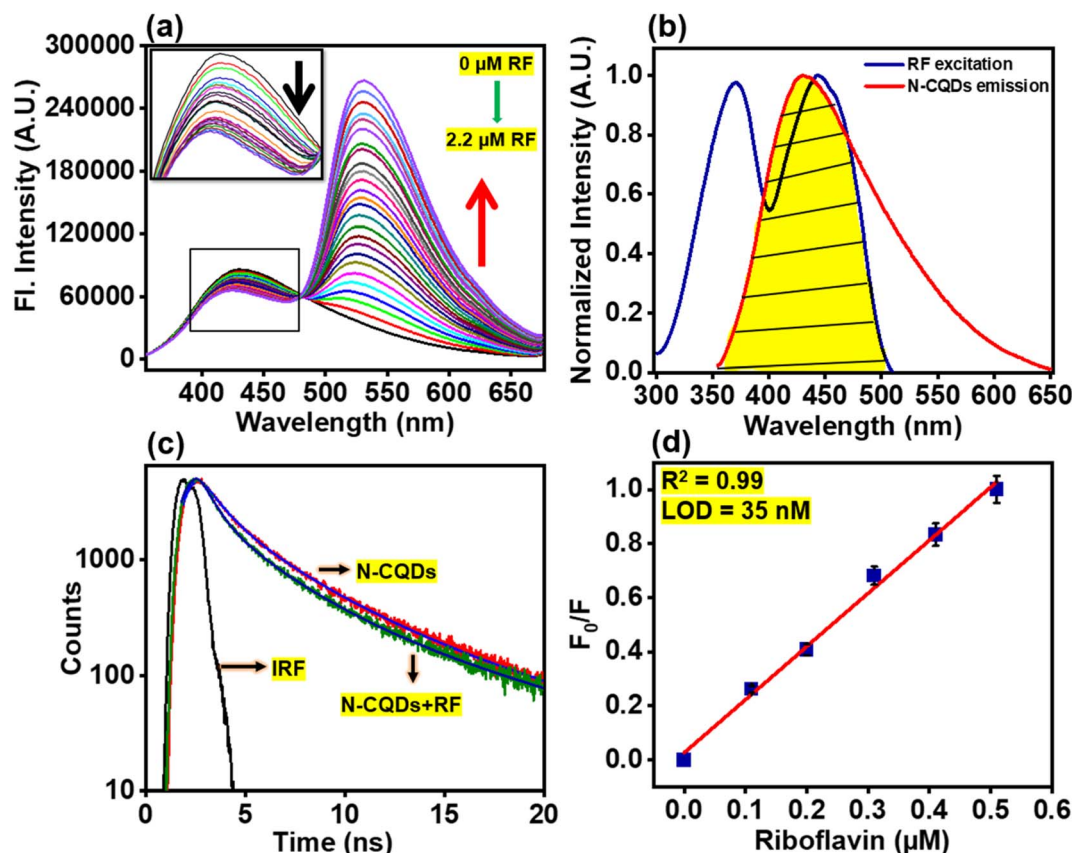
Fig. 5 (a) Variation in fluorescence spectra of N-CQDs in the presence of different concentrations of RF (0–2.2 μM) with the inset image showing fluorescence quenching in aqueous medium. The black arrow depicts the progressive decrease of fl. intensity of N-CQDs at shorter emission wavelength, while a steady increase at longer emission wavelength is represented by the red arrow, (b) spectral overlap between the emission spectrum of N-CQDs (red) and the excitation spectrum of RF (blue) where the yellow color demonstrates the overlapped region in an aqueous medium, (c) fluorescence lifetime decays of N-CQDs in an aqueous medium where, the sharp, thin black line represents the instrument response function, the red and olive lines represent the actual intensity decays in the absence and presence of RF respectively. The blue and royal blue lines correspond to fits obtained in the absence and presence of RF, respectively using a tri-exponential function (see eqn (3); Experimental section), (d) linear relationship of the fluorescence response (F_0/F) of N-CQDs at $\lambda_{em.} = 430$ nm with different concentrations of RF (0–2.2 μM; the red line indicates the linear fit of the data using OriginPro 2021). Error bars represent standard error of measurements obtained from three independent experiments.

Table 2 Analytical performance data for RF (vitamin B_2) sensing using N-CQDs[a]

Parameters	N-CQDs + RF in aqueous medium	N-CQDs + RF in HEPES buffer medium at pH 7.4	N-CQDs + real sample of vitamin B_2 tablet
Linearity range (μM)	0–2.2	0–2.2	0–2.2
Limit of detection (LOD) (nM)	35	55	61
Limit of quantification (LOQ) (nM)	118	186	205
Binding constant (K_1) $(μM^{-1})$	1.65×10^4	1.70×10^4	1.62×10^4
Quenching constant (K_{sv}) $(μM^{-1})$	1.97	1.99	2.00
Regression coefficient (R^2)	0.99	0.99	0.99

[a] Error limit = ±5%.

output, while the other compounds did not show any appreciable changes in N-CQD fluorescence intensity. The selectivity of N-CQDs for RF is based on the energy transfer that occurs only between these two moieties.[5,61–63] The FRET mechanism is operative between N-CQDs and RF (vitamin B_2) as clearly demonstrated due to a substantial overlap (Fig. 5b) between the

emission of the donor (N-CQDs) and excitation of the acceptor (RF) probes. Energy transfer occurs as a result of long range dipole–dipole interactions between the donor and acceptor. Table 3 further clearly depicts that the separation distance between the donor and acceptor is between 1 and 2 nm so FRET is highly effective during sensing.[10] In all the cases, the findings

Table 3 FRET parameters of the N-CQDs@RF nanosensor in different systems

N-CQDs + RF	R_0 (nm)	r (nm)	E (%)
N-CQDs + RF in aqueous medium	1.64	1.80	0.31
N-CQDs + RF in HEPES buffer at pH 7.4	1.77	2.04	0.30
N-CQDs + real sample of vitamin B_2 tablet	1.35	1.57	0.29

demonstrated that the PL intensity of N-CQDs progressively decreased at shorter emission wavelengths, while steadily increasing at longer emission wavelengths. The quenching and enhancement of PL intensity at shorter and longer wavelengths were attributed to the donor fluorescence of N-CQDs and acceptor fluorescence of RF, respectively. The appearance of an isoemissive point in the PL spectra signified the formation of a complex between N-CQDs and RF (vitamin B_2). The outcome clearly demonstrated that the FRET mechanism is operative between N-CQDs and RF (vitamin B_2) due to a substantial overlap (Fig. 5b) between the emission of donor (N-CQDs) and excitation of acceptor (RF) probes. A similar characteristic FRET mechanism also occurs in pH 7.4 buffer (Fig. S7a†) and also upon addition of the real sample of vitamin B_2 supplements (Fig. S7b†). Additionally, time-resolved fluorescence emission studies were carried out by exciting the respective samples at λ_{ex} = 340 nm. The lifetime components (τ_i), relative amplitudes (α_i) and the mean lifetime values (τ_m) are tabulated in Table S2.† The mean lifetime values of N-CQDs were considerably reduced in the presence of RF in aqueous and buffer environments as well as real samples of vitamin B_2 supplements (Tables 1 and S2†), confirming that FRET indeed occurs between electron-rich donor N-CQDs and electron-deficient RF (vitamin B_2) (Fig. 5c, S7c, d, and Scheme 2). In light of this, the proposed nanosensor provided a simple method for developing a ratiometric FRET mechanism for the determination of RF (vitamin B_2) in aqueous and buffer environments.

To gain more insights into the NCQD-RF FRET process, overlap integral [$J(\lambda)$] values were calculated between emission of N-CQDs and excitation of RF using the following equation:[10]

$$J(\lambda) = \frac{\int_0^\infty F_D(\lambda)\varepsilon_A(\lambda)\lambda^4 d\lambda}{\int_0^\infty F_D(\lambda) d\lambda} \quad (9)$$

'$F_D(\lambda)$' represents the corrected fluorescence emission of the donor (D) in the wavelength range λ to $\lambda + \Delta\lambda$ with the total fluorescence intensity (area under the curve), and '$\varepsilon_A(\lambda)$' denotes molar extinction coefficient of the acceptor (A) at wavelength λ. Moreover, the Förster distance (R_0) for the N-CQDs–RF pair was also calculated with the help of the following equation:[10]

$$R_0 = 0.211[\kappa^2 \eta^{-4} \Phi_D J(\lambda)]^{1/6} \quad (10)$$

The term 'κ^2' represents the relative orientation factor of transition dipoles between the donor and acceptor in an isotropic solution. The value of κ^2 for an isotropic solution was considered as 2/3, 'η' denotes the relative viscosity of the medium, and 'ϕ_D' signifies the fluorescence quantum yield value of the donor molecule *i.e.* N-CQDs. The calculated 'R_0' values for the specific N-CQDs–RF pair in an aqueous medium, HEPES buffer medium at pH 7.4 and real samples of vitamin B_2 supplements were found to be <10 nm (tabulated in Table 3), which obeys classical FRET theory and confirmed efficient energy transfer between N-CQDs and RF.[3,10]

Moreover, to estimate the rate of electron transfer (k_{ET}), the following equation was employed:[6]

$$k_{ET} = \frac{1}{\tau_{DA}} - \frac{1}{\tau_D} \quad (11)$$

The parameters 'τ_{DA}' and 'τ_D' symbolize the mean lifetimes of N-CQDs in the presence and absence of RF, respectively. The calculated value of 'k_{ET}' is tabulated in Table 1, indicating that the electron transfer process is favored between N-CQDs and RF. Furthermore, to decipher the nature of the electron transfer mechanism, the FRET efficiency (E) of the N-CQDs–RF nanosensor was calculated using the following equation:[10]

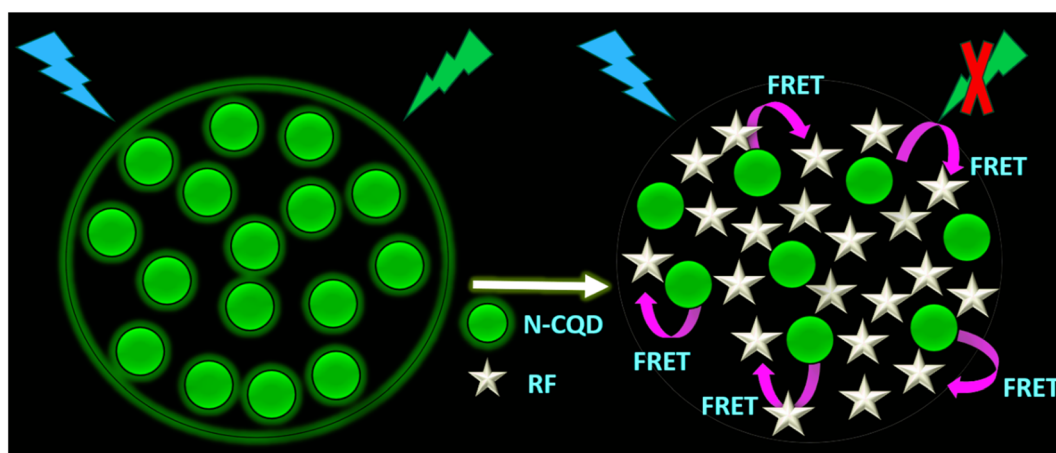$$E = \frac{k_{ET}}{k_r + k_{ET} + k_{nr}} \quad (12)$$

Scheme 2 Schematic representation of the FRET mechanism between N-CQDs and RF leading to quenching of fluorescence emission from N-CQDs.

Table 4 A comparative analysis of LOD for the detection of RF using different nanosensors

Method	Linear range (μM)	Limit of detection (nM)	Reference
NPCDs/riboflavin/FRET system	0.5–50	170	4
Graphitic carbon nitride/fluorimetry (FRET)	0.4–1.0	170	55
Graphene-PEG/fluorescence quenching	0–6.3	90	56
AHNPs/riboflavin/FRET system	0–0.7	71	57
This work	0–2.2	35	—

Table 3 clearly confirms that the FRET efficiency of N-CQDs with RF (vitamin B_2) corroborated well with real sample analysis. Moreover, the separation distance (r) between the N-CQDs–RF was also determined from the respective FRET efficiency values by using the following formula:[10]

$$E = \frac{1}{1 + \left(\dfrac{r}{R_0}\right)^6} \tag{13}$$

The calculated separation distance (r) values (Table 3) are found to be within the range of 1.57–2.04 nm (<10 nm), directly supporting the FRET process between N-CQDs and RF (vitamin B_2).

3.8. Estimation of the limit of detection

An effective nanosensor for practical applications must have high selectivity and sensitivity for the detection of analytes. The limit of detection (LOD) and limit of quantification (LOQ) include the parameters for the sensitivity of an ideal nanosensor. The LOD and LOQ values of the N-CQDs@RF nanosensor in aqueous physiological buffer medium and real samples of vitamin B_2 tablets (Table 2) were calculated from a linear plot between PL responses (F_0/F) and different concentrations of RF (0–2.2 μM) using the values of ($3\sigma/K$) and ($10\sigma/K$), respectively.[23] The parameter 'σ' denoted the standard deviation of the intercept and 'K' is the slope of the respective graphs. The LOD values of RF (vitamin B_2) in the presence of aqueous and buffer medium were found to be ~35 nM (Fig. 5d) and ~56 nM (Fig. S8a†), respectively with a linear concentration range of 0–2.2 μM along with an excellent regression coefficient value of $R^2 = 0.99$. In comparison to other nanosensors reported in the literature, Table 4 demonstrates that the developed nanosensor has a high sensitivity towards RF (vitamin B_2) and a comparatively lower detection limit. The findings clearly suggest that the developed nanoprobe sensitively detects RF in the nanomolar range both in aqueous and physiological buffer environments.

3.9. Method validation with real samples of vitamin B_2

The proposed nanosensor model was validated in accordance with ICHQ2(R1) recommendations.[64] To validate the efficacy of the designed nanosensor, the study was also executed for commercially available vitamin B_2 tablets using the standard addition method. In the real sample, the LOD value was found to be ~61 nM (Fig. S8b†). The synthesized nanoprobe detected an excellent amount of RF with the LOD in the nanomolar range in a real sample of vitamin B_2 tablets (Table S3†), with good recovery percentages and a relative standard deviation (RSD) lower than 4%, indicating the reliability and standard precision and accuracy of ratiometric fluorescent nanosensor based detection of RF (vitamin B_2) in real samples.

4. Conclusions

In summary, using a microwave-assisted pyrolysis technique, a rapid, cost-effective, and sustainable strategy was employed to synthesize N-CQDs from Indian gooseberry (*Phyllanthus emblica*). Presence of amino acids, polyphenols, alkaloids, and cholesterol in the biomass precursor of Indian gooseberry resulted in intrinsic functionalized N-CQDs with high fluorescence properties (PLQY 48%). The synthetic methodology was maintained in a green environment without the use of any harsh chemicals. The presence of nitrogen functionalization on N-CQDs was confirmed by EDS, XPS, FTIR and Raman spectroscopic analysis. HRTEM imaging revealed the spherical shape of the as-prepared nanoprobe with an average diameter of 8.1 nm. N-CQDs showed green emissive fluorescence under UV-illumination and excitation-dependent emission properties. With the aid of UV-visible, fluorescence, and time-resolved emission spectroscopic analysis, the optical properties of N-CQDs were characterized. In addition, N-CQDs also showed remarkable solubility in aqueous and physiological pH of buffer media, photostability, and environmental stability (pH, ionic strength) in order to fulfill the requirements of an ideal nanosensor. The as-prepared nanoprobe showed selectivity and sensitivity towards the detection of RF through the FRET mechanism in the nanomolar range under both aqueous and physiological conditions. The proposed model of the nanosensor was also validated in real samples of vitamin B_2 supplements with high precision and accuracy levels in nanomolar level detection. Therefore, the development of the synthesized nanosensor from biomass may have potential applications in the biological and food industries.

Conflicts of interest

The authors affirm that they have no known financial or interpersonal conflicts that would have appeared to have an impact on the research presented in this study.

Acknowledgements

References

1 A. Kundu, S. Nandi, R. K. Layek and A. K. Nandi, *ACS Appl. Mater. Interfaces*, 2013, **5**, 7392–7399, DOI: **10.1021/am4017208**.

2 S. Pramanik, S. Roy and S. Bhandari, *Nanoscale Adv.*, 2020, **2**, 3809–3814, DOI: **10.1039/D0NA00540A**.

3 S. S. Monte-Filho, S. I. E. Andrade, M. B. Lima and M. C. U. Araujo, *J. Pharm. Anal.*, 2019, **9**, 209–216, DOI: **10.1016/j.jpha.2019.02.003**.

4 L. Lin, Y. Wang, Y. Xiao and X. Chen, *Anal. Chem.*, 2019, **411**, 2803–2808, DOI: **10.1007/s00216-019-01725-1**.

5 R. Sotolongo-García, R. Rodríguez-Velázquez, M. Alatorre-Meda, M. T. Oropeza-Guzmán, A. Tirado-Guízar and G. Pina-Luis, *Nanomaterials*, 2021, **11**, 1981–1999, DOI: **10.3390/nano11081981**.

6 R. Qiang, S. Yang, K. Hou and J. Wang, *New J. Chem.*, 2019, **43**, 10826–10833, DOI: **10.1039/c9nj02291k**.

7 S. Y. Lim, W. Shen and Z. Gao, *Chem. Soc. Rev.*, 2015, **44**, 362–381, DOI: **10.1039/c4cs00269e**.

8 L. Hu, X. Yang, C. Wang, H. Yuan and D. Xiao, *J. Chromatogr. B*, 2007, **856**, 245–251, DOI: **10.1016/j.jchromb.2007.06.011**.

9 M. Zandomeneghi, L. Carbonaro, L. Calucci, C. Pinzino, L. Galleschi and S. Ghiringhelli, *J. Agric. Food Chem.*, 2003, **51**, 2888–2895, DOI: **10.1021/jf0260287**.

10 J. R. Lakowicz, *Principles of Fluorescence Spectroscopy*, Springer, New York, 3rd edn, 2006, 1–95 and 529–575.

11 W. Dong, R. Wang, X. Gong and C. Dong, *Anal. Bioanal. Chem.*, 2019, **411**, 6687–6695, DOI: **10.1007/s00216-019-02042-3**.

12 T. H. Le, Y. N. Ahn and S. J. Park, *Korean J. Chem. Eng.*, 2022, **39**, 1065–1071, DOI: **10.1007/s11814-021-0956-4**.

13 Q. Zhao, W. Song, B. Zhao and B. Yang, *Mater. Chem. Front.*, 2020, **4**, 472–488, DOI: **10.1039/c9qm00592g**.

14 F. Yan, Z. Sun, H. Zhang, X. Sun, Y. Jiang and Z. Bai, *Microchim. Acta*, 2019, **186**, 583–620, DOI: **10.1007/s00604-019-3688-y**.

15 P. Kumar, S. Dua, R. Kaur, M. Kumar and G. Bhatt, *RSC Adv.*, 2022, **12**, 4714–4759, DOI: **10.1039/d1ra08452f**.

16 S. Ramírez-Barroso, A. Jacobo-Martín, I. Navarro-Baena, J. J. Hernández, C. Navio, I. Rodríguez and R. Wannemacher, *J. Mater. Chem. C*, 2021, **9**, 16935–16944, DOI: **10.1039/D1TC04255F**.

17 S. Anwar, H. Ding, M. Xu, X. Hu, Z. Li, J. Wang, L. Liu, L. Jiang, D. Wang, C. Dong, M. Yan, Q. Wang and H. Bi, *ACS Appl. Bio Mater.*, 2019, **2**, 2317–2338, DOI: **10.1021/acsabm.9b00112**.

18 H. Li, Z. Kang, Y. Liu and S. T. Lee, *J. Mater. Chem.*, 2012, **22**, 24230–24253, DOI: **10.1039/C2JM34690G**.

19 M. K. Barman and A. Patra, *J. Photochem. Photobiol., C*, 2018, **37**, 1–22, DOI: **10.1016/j.jphotochemrev.2018.08.001**.

20 P. K. Yadav, V. K. Singh, S. Chandra, D. Bano, V. Kumar, M. Talat and S. H. Hasan, *ACS Biomater. Sci. Eng.*, 2019, **5**(2), 623–632, DOI: **10.1021/acsbiomaterials.8b01528**.

21 M. Park, A. Sharma, C. Kang, J. Han, K. M. Tripathi and H. Lee, *ACS Biomater. Sci. Eng.*, 2022, **8**(5), 2131–2141, DOI: **10.1021/acsbiomaterials.1c01598**.

22 W. Deng, C. Zang, Q. Li, B. Sun, X. Mei, L. Bai, X. Shang, Y. Deng, Y. Xiao, R. Ghiladi, G. Lorimer, X. Zhang and J. Wang, *ACS Biomater. Sci. Eng.*, 2023, **9**(3), 1307–1319, DOI: **10.1021/acsbiomaterials.2c01537**.

23 A. Kundu, B. Maity and S. Basu, *ACS Biomater. Sci. Eng.*, 2022, **8**(11), 4764–4776, DOI: **10.1021/acsbiomaterials.2c00798**.

24 R. Atchudan, S. C. Kishore, P. Gangadaran, T. N. J. I. Edison, S. Perumal, R. L. Rajendran, M. Alagan, S. Al-Rashed, B. C. Ahn and Y. R. Lee, *Environ. Res.*, 2022, **204**, 112365, DOI: **10.1016/j.envres.2021.112365**.

25 R. Atchudan, T. N. J. I. Edison, S. Perumal, N. Muthuchamy and Y. R. Lee, *Fuel*, 2020, **275**, 117821–117830, DOI: **10.1016/j.fuel.2020.117821**.

26 R. Atchudan, T. N. J. I. Edison, S. Perumal, R. Vinodh and Y. R. Lee, *J. Mol. Liq.*, 2019, **296**, 111817–111826, DOI: **10.1016/j.molliq.2019.111817**.

27 R. Atchudan, T. N. J. I. Edison, K. R. Aseer, S. Perumal, N. Karthik and Y. R. Lee, *Biosens. Bioelectron.*, 2018, **99**, 303–311, DOI: **10.1016/j.bios.2017.07.076**.

28 R. Atchudan, T. N. J. I. Edison and Y. R. Lee, *J. Colloid Interface Sci.*, 2016, **482**, 8–18, DOI: **10.1016/j.jcis.2016.07.058**.

29 K. V. Kulkarni and S. M. Ghurghure, *Int. J. Chem. Stud.*, 2018, **2**, 5–11, DOI: **10.22207/JPAM.13.4.11**.

30 S. Shrivastava, J. Kaur, M. Mehraj, F. Feroz, J. Chawla and S. Kumari, *J. Pharm. Innov.*, 2022, **11**, 6–16.

31 V. Arul and M. G. Sethuraman, *ACS Omega*, 2019, **4**, 3449–3457, DOI: **10.1021/acsomega.8b03674**.

32 R. Atchudan, T. N. J. I. Edison, S. Perumal and Y. R. Lee, *ACS Omega*, 2018, **3**, 17590–17601, DOI: **10.1021/acsomega.8b02463**.

33 K. Jlassi, K. Eid, M. H. Sliem, A. M. Abdullah, M. M. Chehimi and I. Krupa, *Environ. Sci. Eur.*, 2020, **32**, 12–25, DOI: **10.1186/s12302-020-0292-z**.

34 M. Wang, Y. Wan, K. Zhang, Q. Fu, L. Wang, J. Zeng, Z. Xia and D. Gao, *Anal. Bioanal. Chem.*, 2019, **411**, 2715–2727, DOI: **10.1007/s00216-019-01712-6**.

35 P. Thirukumaran, R. Atchudan, R. Balasubramanian, A. Shakila Parveen and S. C. Kim, *Int. J. Hydrogen Energy*, 2018, **43**, 13266–13275, DOI: **10.1016/j.ijhydene.2018.05.108**.

36 Y. Hu, J. Yang, J. Tian, L. Jia and J. S. Yu, *Carbon*, 2014, **77**, 775–782, DOI: **10.1016/j.carbon.2014.05.081**.

37 A. F. Shaikh, M. S. Tamboli, R. H. Patil, A. Bhan, J. D. Ambekar and B. B. Kale, *J. Nanosci. Nanotechnol.*, 2019, **19**, 2339–2345, DOI: **10.1166/jnn.2019.16537**.

38 A. Alhaidrai SA, A. Hadi-FA, A. Kaf AG and T. A. Deen AM, *Bioequivalence Bioavailab. Int. J.*, 2022, **6**(2), 000179–000187, DOI: **10.23880/beba-16000179**.

39 Z. Hu, X. Y. Jiao and L. Xu, *Microchem. J.*, 2020, **154**, 104588–104596, DOI: **10.1016/j.microc.2019.104588**.

40 W. U. Khan, D. Wang, W. Zhang, Z. Tang, X. Ma, X. Ding, S. Du and Y. Wang, *Sci. Rep.*, 2017, **7**, 14866–14875, DOI: **10.1038/s41598-017-15054-9**.

41 Y. Xie, D. Cheng, X. Liu and A. Han, *Sensors*, 2019, **19**, 3169–3179, DOI: **10.3390/s19143169**.

42 S. Sahu, B. Behera, T. K. Maiti and S. Mohapatra, *Chem. Commun.*, 2012, **48**, 8835–8837, DOI: **10.1039/C2CC33796G**.

43 O. Akhavan, *Carbon*, 2015, **81**, 158–166, DOI: **10.1016/j.carbon.2014.09.044**.

44 R. Atchudan, T. N. J. I. Edison, S. Perumal, N. Karthik, D. Karthikeyan, M. Shanmugam and Y. R. Lee, *J. Photochem. Photobiol., A*, 2018, **305**, 75–85, DOI: **10.1016/j.jphotochem.2017.09.038**.

45 Z. M. S. H. Khan, R. S. Rahman, Shumaila, S. Islam and M. Zulfequar, *Opt. Mater.*, 2019, **91**, 386–395, DOI: **10.1016/j.optmat.2019.03.054**.

46 R. Atchudan, T. N. J. I. Edison, M. Shanmugam, S. Perumal, T. Somanathan and Y. R. Lee, *Phys. E*, 2021, **126**, 114417, DOI: **10.1016/j.physe.2020.114417**.

47 W. Zhao, Y. Zhang, B. Cao, Z. Li, C. Sun, X. Cao and S. Cong, *Foods*, 2022, **11**, 2451–2465, DOI: **10.3390/foods11162451**.

48 M. Bai, W. Wu, L. Liu, J. Chen, X. Ma and Y. J. Meng, *Nanopart. Res.*, 2019, **21**, 145–158, DOI: **10.1007/s11051-019-4574-6**.

49 S. Kainth, N. Goel, S. Basu and B. Maity, *New J. Chem.*, 2022, **46**(2), 686–694, DOI: **10.1039/D1NJ04838D**.

50 X. Ma, S. Li, V. Hessel, L. Lin, S. Meskers and F. Gallucci, *Chem. Eng. Process.*, 2019, **140**, 29–35, DOI: **10.1016/j.cep.2019.04.017**.

51 K. Kamalakannan, A. Morais, I. Nongwe, C. Longo, A. F. Nogueira and N. J. Coville, *J. Mol. Catal. A: Chem.*, 2016, **422**, 165–174, DOI: **10.1016/j.molcata.2015.10.024**.

52 P. S. R. Prasad, K. S. Prasad and N. K. Thakur, *Curr. Sci.*, 2006, **90**, 1544–1547.

53 A. Kumari, A. Kumar, A. K. Sahu and S. Kumar, *Sens. Actuators, B*, 2018, **254**, 197–205, DOI: **10.1016/j.snb.2017.07.075**.

54 Y. Deng, M. Chen, G. Chen, W. Zou, Y. Zhao, H. Zhang and Q. Zhao, *ACS Omega*, 2021, **6**(6), 4247–4254, DOI: **10.1021/acsomega.0c05182**.

55 T. K. Mondal, U. K. Ghorai and S. K. Saha, *ACS Omega*, 2018, **3**, 11439–11446, DOI: **10.1021/acsomega.8b01159**.

56 L. Wang, S. Weng, S. Su and W. Wang, *RSC Adv.*, 2023, **13**, 19173–19194, DOI: **10.1039/D3RA02519E**.

57 A. Dager, T. Uchida, T. Maekawa and M. Tachibana, *Sci. Rep.*, 2019, **9**, 14004–14016, DOI: **10.1038/s41598-019-50397-5**.

58 N. Sohal, B. Maity and S. Basu, *ACS Appl. Bio Mater.*, 2022, **5**(5), 2355–2364, DOI: **10.1021/acsabm.2c00189**.

59 L. F. Russell, L. Brooks and K. B. McRae, *Food Chem.*, 1998, **63**, 125–131, DOI: **10.1016/S0308-8146(97)00216-1**.

60 R. R. Eitenmiller, W. O. Landen Jr and L. Ye, *Vitamin Analysis for the Health and Food Sciences*, CRC Press, Boca Raton, 2nd edn, 2008, DOI: **10.1201/9781420009750**.

61 J. Han, H. Y. Zou, M. X. Gao and C. Z. Huang, *Talanta*, 2016, **148**, 279–284, DOI: **10.1016/j.talanta.2015.10.038**.

62 A. M. Díez-Pascual, D. García-García, M. P. San Andrés and S. Vera, *RSC Adv.*, 2016, **6**, 19686–19699, DOI: **10.1039/C5RA25547C**.

63 P. G. Mahajan, N. C. Dige, S. B. Suryawanshi, D. K. Dalavi, A. A. Kamble, D. P. Bhopate, A. N. Kadam, V. V. Kondalkar, G. B. Kolekar and S. R. Patil, *J. Fluoresc.*, 2018, **28**, 207–215, DOI: **10.1007/s10895-017-2183-2**.

64 I. C. H. H. T. Guideline, *Validation of Analytical Procedures: Text and Methodology, Q2(R1)*, 2005, vol. 20, p. 5.